Monthly Notices of the ROYAL ASTRONOMICAL SOCIETY

MNRAS **521,** 3517–3526 (2023) https://doi.org/10.1093/mnras/stad746
Advance Access publication 2023 March 16

# TESS shines light on the origin of the ambiguous nuclear transient ASASSN-18el

Jason T. Hinkle ,[1★] Christopher S. Kochanek ,[2,3] Benjamin J. Shappee,[1] Patrick J. Vallely,[2] Katie Auchettl,[4,5,6] Michael Fausnaugh,[7] Thomas W.-S. Holoien ,[8†] Helena P. Treiber ,[1,9] Anna V. Payne,[1‡] B. Scott Gaudi,[2] Keivan G. Stassun ,[10] Todd A. Thompson ,[2,3] J. L. Tonry[1] and Steven Villanueva, Jr[11§]

[1] Institute for Astronomy, University of Hawai'i, 2680 Woodlawn Dr, Honolulu, HI 96822, USA
[2] Department of Astronomy, The Ohio State University, 140 West 18th Avenue, Columbus, OH 43210, USA
[3] Center for Cosmology and Astroparticle Physics, The Ohio State University, 191 W. Woodruff Avenue, Columbus, OH 43210, USA
[4] School of Physics, The University of Melbourne, Parkville, VIC 3010, Australia
[5] ARC Centre of Excellence for All Sky Astrophysics in 3 Dimensions (ASTRO 3D), Sydney, NSW 2006, Australia
[6] Department of Astronomy and Astrophysics, University of California, Santa Cruz, CA 95064, USA
[7] Department of Physics and Kavli Institute for Astrophysics and Space Research, Massachusetts Institute of Technology, Cambridge, MA 02139, USA
[8] The Observatories of the Carnegie Institution for Science, 813 Santa Barbara St., Pasadena, CA 91101, USA
[9] Department of Physics and Astronomy, Amherst College, C025 New Science Center, 25 East Dr, Amherst, MA 01002-5000, USA
[10] Department of Physics and Astronomy, Vanderbilt University, Nashville, TN 37235, USA
[11] NASA Goddard Space Flight Center, Exoplanets and Stellar Astrophysics Laboratory (Code 667), Greenbelt, MD 20771, USA

Accepted 2023 March 5. Received 2023 February 22; in original form 2022 June 28

## ABSTRACT

We analyse high-cadence data from the Transiting Exoplanet Survey Satellite (*TESS*) of the ambiguous nuclear transient (ANT) ASASSN-18el. The optical changing-look phenomenon in ASASSN-18el has been argued to be due to either a drastic change in the accretion rate of the existing active galactic nucleus (AGN) or the result of a tidal disruption event (TDE). Throughout the *TESS* observations, short-time-scale stochastic variability is seen, consistent with an AGN. We are able to fit the *TESS* light curve with a damped-random-walk (DRW) model and recover a rest-frame variability amplitude of $\hat{\sigma} = 0.93 \pm 0.02$ mJy and a rest-frame time-scale of $\tau_{DRW} = 20^{+15}_{-6}$ d. We find that the estimated $\tau_{DRW}$ for ASASSN-18el is broadly consistent with an apparent relationship between the DRW time-scale and central supermassive black hole mass. The large-amplitude stochastic variability of ASASSN-18el, particularly during late stages of the flare, suggests that the origin of this ANT is likely due to extreme AGN activity rather than a TDE.

**Key words:** accretion, accretion discs – black hole physics – galaxies: active – galaxies: nuclei.

## 1 INTRODUCTION

Active galactic nuclei (AGNs) are the actively accreting supermassive black holes (SMBHs) found at the centre of ∼1–5 per cent of galaxies in the local universe (e.g. Ho 2008; Haggard et al. 2010; Lacerda et al. 2020). For decades, it has been known that AGNs vary stochastically both photometrically (e.g. Ulrich, Maraschi & Urry 1997; Drake et al. 2009; MacLeod et al. 2012) and spectroscopically (e.g. Bianchi et al. 2005). Due to the recent growth of optical transient surveys, AGNs and quiescent galaxies alike have also been found to undergo extreme flaring behaviour. Such events include tidal disruption events (TDEs; van Velzen et al. 2011; Gezari et al. 2012; Holoien et al. 2014b, 2016a; Payne et al. 2021; Hinkle et al. 2021b), dramatic changes in the accretion rates of known AGNs (e.g. Denney et al. 2014; Shappee et al. 2014; Wyrzykowski et al. 2017; Frederick et al. 2019; Trakhtenbrot et al. 2019a; Frederick et al. 2021), and a growing class of ambiguous nuclear transients (ANTs; Neustadt et al. 2020; Holoien et al. 2021; Hinkle et al. 2021a).

Broadly, nuclear transients share a set of observed characteristics including bright ultraviolet (UV) emission (e.g. Holoien et al. 2016a; Neustadt et al. 2020; Hinkle et al. 2021a), strong emission lines (Holoien et al. 2014b; Leloudas et al. 2019; Trakhtenbrot et al. 2019a), slow and often smooth photometric evolution (Hinkle et al. 2020; Frederick et al. 2021; van Velzen et al. 2021), and, for some events, X-ray emission (Holoien et al. 2016a; Neustadt et al. 2020; Hinkle et al. 2021b). The different classes of nuclear transients often have distinct properties in their X-ray continua, colour evolution, and the presence of light-curve rebrightening episodes (e.g. Frederick et al. 2021). However, in the case of ANTs, the lack of expected features or the presence of unexpected features can make a definitive classification difficult (Neustadt et al. 2020; Frederick et al. 2021; Holoien et al. 2021; Malyali et al. 2021; Hinkle et al. 2021a).

★ E-mail: jhinkle6@hawaii.edu
† NHFP Einstein Fellow.
‡ NASA Fellowship Activity Fellow.
§ NPP Fellow.

One example of an ANT is ASASSN-18el (AT2018zf[1]; Nicholls et al. 2018; Trakhtenbrot et al. 2019b). ASASSN-18el, ($\alpha$, $\delta$) = (19:27:19.630, +65:33:53.78), was discovered by the All-Sky Automated Survey for Supernovae (ASAS-SN; Shappee et al. 2014; Kochanek et al. 2017) on 2018 March 3 in a known AGN, 1ES 1927 + 654 (Giacconi et al. 1979). Archival spectra were that of a 'true' Type 2 AGN, with narrow lines and no broad lines even in polarized light (Boller et al. 2003; Tran, Lyke & Mader 2011). Pre-discovery imaging from the Asteroid Terrestrial-impact Last Alert System (ATLAS; Tonry et al. 2018a) indicates that the source became active as early as 2017 December 23 (Trakhtenbrot et al. 2019b).

Spectroscopic follow-up of the flare found that the AGN had broad emission lines, suggesting that ASASSN-18el was an optical changing-look AGN (CL-AGN; e.g. Denney et al. 2014; Shappee et al. 2014; LaMassa et al. 2015), changing from a Seyfert 2 to a Seyfert 1 over the course of several months. During the optical flare, the X-ray flux dropped by several orders of magnitude (Trakhtenbrot et al. 2019b; Ricci et al. 2021; Laha et al. 2022) and the dominant X-ray component softened from a hard power-law typical of an AGN (e.g. Ricci et al. 2017) to a more TDE-like blackbody spectrum (e.g. Auchettl, Guillochon & Ramirez-Ruiz 2017). Based on the X-ray evolution and smooth UV/optical flare, Ricci et al. (2020) speculated that ASASSN-18el was a TDE. None the less, the overall properties of ASASSN-18el make a definitive distinction between an AGN flare and TDE difficult.

In this paper, we analyse photometry of ASASSN-18el from the Transiting Exoplanet Survey Satellite (*TESS*; Ricker et al. 2015), additional late-time optical light curves, and late-time X-ray light curves from the Neutron Star Interior and Composition Explorer (*NICER*; Gendreau, Arzoumanian & Okajima 2012) to understand the emission of ASASSN-18el in the growing context of nuclear flares. This paper is organized as follows. In Section 2, we detail the data used in this work. In Section 3, we present our analysis and then discuss our results in Section 4. Finally, we summarize our findings in Section 5. Throughout the paper, we assume a cosmology of $H_0 = 69.6$ km s$^{-1}$ Mpc$^{-1}$, $\Omega_M = 0.29$, and $\Omega_\Lambda = 0.71$ (Wright 2006; Bennett et al. 2014). The source redshift of z = 0.01905 implies a luminosity distance of 83.3 Mpc and the Galactic foreground extinction in the direction of ASASSN-18el is $A_V = 0.236$ mag Schlafly & Finkbeiner (2011). Trakhtenbrot et al. (2019b) measured a virial mass of $M_{BH} = 1.9 \times 10^7$ M$_\odot$ using spectra from their follow-up campaign, which we adopt in this manuscript. As this is a single epoch measurement, we will assume an uncertainty of 0.3 dex (e.g. Guo et al. 2020).

## 2 DATA

Data near peak emission and up to roughly 400 d after were presented originally in Trakhtenbrot et al. (2019b), with additional X-ray data shown in Ricci et al. (2021) and X-ray/UV data shown in Laha et al. (2022). Here, we re-reduce ground-based survey data on ASASSN-18el from ASAS-SN and ATLAS, now extending roughly 1300 d after peak. We additionally use TESS, Swift, NICER, and ground-based follow-up data. In this section, we describe the procedures used to obtain and reduce these data.

[1]https://www.wis-tns.org/object/2018zf

### 2.1 ASAS-SN data

The ASAS-SN transient survey consists of five sites located at Haleakalā Observatory, McDonald Observatory, the South African Astrophysical Observatory, and two at Cerro Tololo Inter-American Observatory, all hosted by the Las Cumbres Observatory (Brown et al. 2013). Each site hosts four telescopes on a common mount, and the telescopes are 14-cm aperture Nikon telephoto lenses with 8$''$.0 pixels. However, at the time of the discovery of ASASSN-18el, ASAS-SN operated with two units taking *V*-band images and three units taking *g*-band images. After the seasonal break following the transient peak emission, ASAS-SN had fully switched to *g*-band imaging and all of the later time ASAS-SN data are in the *g*-band.

The images were reduced using the automated ASAS-SN pipeline (Shappee et al. 2014), which uses the ISIS image subtraction package (Alard & Lupton 1998; Alard 2000). We then used the IRAF APPHOT package with a two-pixel radius (approximately 16$''$.0) aperture to perform aperture photometry on each subtracted image to produce a differential light curve. We calibrated our photometry using the AAVSO Photometric All-Sky Survey (Henden et al. 2015). To obtain good detections or limits throughout the transient evolution, we stacked the ASAS-SN epochs. We used 10-d bins prior to and during the flare for both *V*- and *g*-band data, and 50-d bins for the *g*-band data after the seasonal break to sample the decline. We excluded ASAS-SN data more than 1000 d after peak optical emission as contamination from the residuals of a nearby star became similar in amplitude to the transient.

### 2.2 ATLAS data

At the time of discovery, ATLAS consisted of two 0.5-m f/2 Wright Schmidt telescopes located on Haleakalā and at the Mauna Loa Observatory. The ATLAS telescopes typically obtain four 30-s exposures of 200–250 fields, covering roughly a quarter of the sky visible from Hawaii, each night (Smith et al. 2020). Depending on the Moon phase, ATLAS uses either the 'cyan' (*c*) filter from 420–650 nm or the 'orange' (*o*) filter covering the 560–820 nm range (Tonry et al. 2018a). As there was little *c*-band coverage of the flare, particularly in the late phases where we focus our study, we have excluded it from our analysis.

The ATLAS images are processed by a pipeline that includes flat-field, astrometric, and photometric calibrations. We performed forced photometry on the subtracted ATLAS images of ASASSN-18el as described in Tonry et al. (2018a) to create a differential light curve. Due to the bright host galaxy and nearby stars, there are many epochs with artefacts remaining in the subtracted images, as indicated by the high reduced $\chi^2$ of the PSF fits. We therefore excluded images with reduced $\chi^2 > 10$. Similar to our ASAS-SN light curves, we combined individual epochs to increase the S/N. Prior to the flare, we combined the data in 10-d bins, during the flare we combined the four intranight observations, and after the seasonal break we stacked in 30-d bins.

### 2.3 Additional photometry

We also obtained *BVrRiI* data from several ground-based observatories. These include the Las Cumbres Observatory Global Telescope network (Brown et al. 2013), the 0.5-m DEdicated MONitor of EXotransits and Transients (DEMONEXT; Villanueva et al. 2016; Villanueva Steven et al. 2018), the 0.5-m Iowa Robotic Telescope, and the Post Observatory.

We reduced these data using standard procedures including flat-field corrections and then obtained the astrometry for each image using astrometry.net (Barron et al. 2008; Lang et al. 2010). For these ground-based data, we used `apphot` to measure 5″.0 aperture magnitudes of the host plus transient emission and subtracted the 5″.0 host flux computed by Hinkle et al. (2021c). We used REFCAT (Tonry et al. 2018b) magnitudes of stars in the field and the corrections of Lupton (2005) for calibration. We stacked all of this ground-based photometry in 1-d bins as the source was bright, and there were several facilities taking images concurrently.

We also use the Swift *UBV* + *UV* photometry of ASASSN-18el presented in Hinkle et al. (2021c). Some of these data were originally presented in Trakhtenbrot et al. (2019b) but were re-reduced in Hinkle et al. (2021c) to account for corrected calibration files for the Swift UV filters. Fig. 1 shows the light curves of ASASSN-18el from ASAS-SN, ATLAS, Swift, and ground-based observatories in AB magnitudes and corrected for Galactic foreground extinction.

### 2.4 *TESS* observations

The host galaxy of ASASSN-18el lies close to the North Ecliptic Pole and the *TESS* northern continuous viewing zone. It was observed in each sector of Cycle 2 except for Sector 24. The source was very close to the edge of the chip in Sector 14, and therefore we do not include this sector. This allowed us to get a high-cadence and high-precision light curve beginning roughly 500 d after the peak optical emission. The source was also observed again in Sectors 40 and 41 of Cycle 4.

The differential light curves are generated from the *TESS* full frame images (FFIs) following the procedures of Vallely et al. (2019, 2021). Because the TESS PSF has non-trival structure and the camera orientations rotate between sectors, we constructed independent reference images for each sector. We selected the first 100 FFIs of good quality obtained in each sector, excluding images with above average sky background levels or PSF widths. We also excluded FFIs that were affected by an instrument anomaly, showed significant backgrounds due to scattered light, had data quality flags, or a compromised spacecraft pointing. We converted the measured fluxes into *TESS*-band magnitudes using an instrumental zero point of 20.44 electrons per second in the FFIs (TESS Instrument Handbook; Vanderspek et al. 2018).

### 2.5 *NICER* observations

Throughout the evolution of ASASSN-18el, X-ray observations were obtained using NICER (Gendreau et al. 2012), an external payload on the International Space Station. NICER observed ASASSN-18el a total of 431 times between 2018 May 22.8 and 2021 February 17.7 (ObsIDs: 1200190101 − 1200190287, 2200190201 − 2200190370, and 3200190301 − 3200190451; PI: Kara).

The NICER data were reduced using NICERDAS version 6a and HEASOFT version 6.26.1. We applied standard filtering criteria in NICERL2. These criteria include[2]: a *NICER* pointing of ANG_DIST <0.015 degrees from the source location and exclusion of events during a South Atlantic Anomaly passage or when Earth was 30° (40°) above the dark (bright) limb. We also removed events that were flagged as overshoot or undershoot events (EVENT_FLAGS = bxxxx00) and used the 'trumpet filter' to remove events with a PI_RATIO > 1.1 + 120/PI (Bogdanov et al. 2019).

[2]See https://heasarc.gsfc.nasa.gov/docs/nicer/data_analysis/nicer_analysis_guide.html or (Bogdanov et al. 2019) for more details.

To extract count rates for each epoch, we used XSELECT, and the standard ancillary response (nixtiaveonaxis20180601v002.arf) and response matrix (nixtiref20170601v001.rmf) files from the *NICER* CALDB. We assumed a photon index of 1.7 and the Galactic column density of $6.4 \times 10^{20}$ cm$^{-2}$ (Ricci et al. 2020) to convert the count rates to fluxes. Data within ∼500 d of peak optical emission were presented in Ricci et al. (2021). Here, we extend the NICER data coverage until nearly 1100 d after peak to trace the X-ray luminosity evolution at late times.

## 3 ANALYSIS

### 3.1 Optical light curve

In addition to the pre-flare and near-peak data presented in Trakhtenbrot et al. (2019b), the light curves shown in Fig. 1 now extend several years after the peak emission of the transient. It is clear that at the beginning of the *TESS* observations of ASASSN-18el, the transient is still detectable in both the stacked ASAS-SN *g*-band and the ATLAS *o*-band data.

To obtain a time of peak optical light, we fit a parabola to the ATLAS *o*-band light curve as it is the most complete on both sides of the peak. Since the cadence is low, we fit the parabola over a wide date range of dates between MJD = 58116.2 and MJD = 58292.5. We generated 10 000 realizations of the ATLAS light curve over this date range with each flux perturbed by its uncertainty assuming Gaussian errors. We then fit a parabola to each of the perturbed light curves and took the median value as the peak of the distribution and used the 16th and 84th percentiles as the uncertainties. This leads to a time of peak *o*-band emission of MJD = 58 210 ± 2 with a peak flux of 1.9 ± 0.1 mJy. Several studies of TDE flares have found significant offsets between the peak times in different optical bands (Holoien et al. 2019, 2020; Hinkle et al. 2021b) although the cadence of ASAS-SN data and the lack of UV data near peak preclude such comparisons.

One distinguishing feature of TDE light curves is that they are commonly described by a power-law decline in flux. In particular, when the mass per unit binding energy is constant, the decline slope is $t^{-5/3}$ (e.g. Evans & Kochanek 1989). To examine the decline slope of ASASSN-18el in the context of TDEs, we fit the ATLAS *o*-band flux as

$$f = f_{10}\left(\frac{t - t_0}{10\ \mathrm{d}}\right)^{\alpha} + h \quad (1)$$

to estimate the time $t_0$, the flux 10 d later $f_{10}$, the flux offset $h$, and the power-law index $\alpha$. We fit the ATLAS data from 10 d after peak to MJD = 58817.5. An MCMC (Markov Chain Monte Carlo) fit yields best-fitting parameters of $t_0$(MJD) = $58101^{+17}_{-14}$, $f_{10} = 28^{+12}_{-10}$ mJy, $h = -0.10^{+0.06}_{-0.09}$ mJy, and $\alpha = -1.05^{+0.15}_{-0.12}$, and this model is shown in Fig. 2. This decline is consistent with the UV decline slope of $\alpha = -0.91 \pm 0.04$ measured by Laha et al. (2022). The decline slope is also significantly flatter than expected for TDEs (e.g. Rees 1988; Phinney 1989), consistent with the qualitative comparison shown in Trakhtenbrot et al. (2019b). In Fig. 2, we also show a $t^{-5/3}$ decline, fit with the same $t_0$ as above. While the $t^{-5/3}$ decline roughly follows the ATLAS photometry, the flatter decline slope of $\alpha = -1.05$ clearly provides a better description of the decline seen for ASASSN-18el.

The root mean squared (RMS) residuals from the power-law fit are 0.11 mJy after subtracting the median ATLAS flux uncertainty (e.g. Vaughan et al. 2003). For the remaining calculations of the RMS

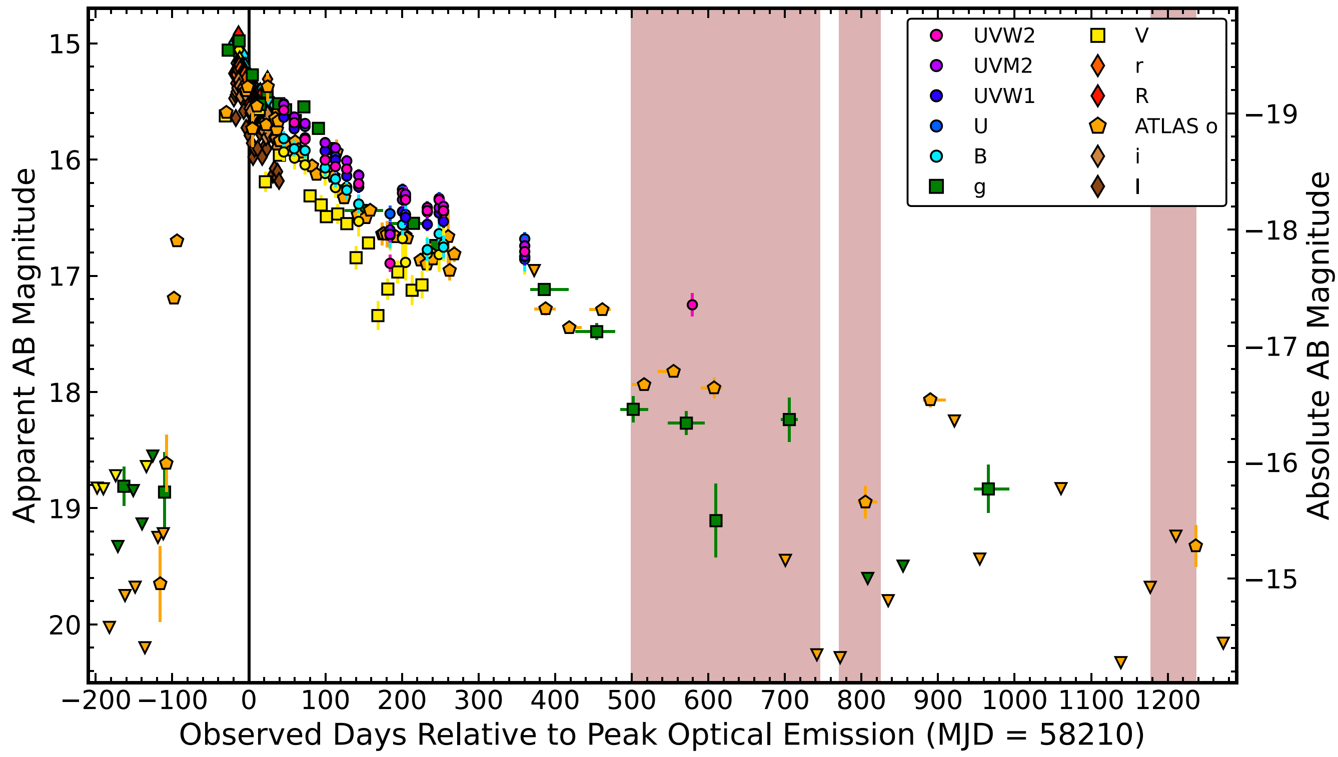


**Figure 1.** Optical and UV light curves of ASASSN-18el, showing ASAS-SN (*gV*; squares), ATLAS (*o*; pentagons), Swift (*UBV* + *UV*; circles), and other ground-based (*BVrRiI*; diamonds) photometry. The photometry shown here spans from roughly 200 d prior to peak optical emission in the ATLAS *o*-band to roughly 1250 d after in observer-frame days. The vertical red bands indicate time periods with *TESS* coverage. The vertical black line indicates the time of the ATLAS *o*-band peak. Horizontal error bars indicate the date range of observations stacked to obtain deeper limits and higher S/N detections, although for some data they are smaller than the symbols. Downward-facing triangles indicate 3$\sigma$ upper limits. All data are corrected for Galactic extinction and are shown in the AB system.

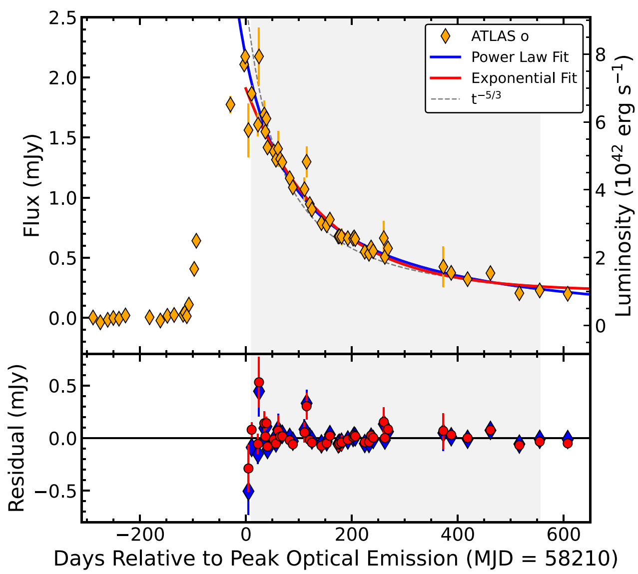


**Figure 2.** *Top panel*: ATLAS *o*-band light curve (orange diamonds) and the best-fitting power-law (exponential-decay) model in blue (red). The light grey shaded region shows the time period included in the fits. Also shown with the dashed grey line is a $t^{-5/3}$ decline assuming the same $t_0$ as the free index power-law fit. *Bottom panel*: The residuals of the models, shown in the same colour as the fits themselves.

scatter, we subtract the median flux uncertainty to correct for the contribution of statistical noise to the observed variability.

We next fit the decline of ASASSN-18el using an exponential-decay model

$$f = ae^{-(t-t_{peak})/\tau_{decay}} + c \quad (2)$$

similar to what has been done for some TDEs (e.g. Holoien et al. 2014a, 2016a, b; Payne et al. 2021). Here, we set $t_{peak}$ of MJD = 58 210 from our fit to the ATLAS *o*-band light curve and fit the ATLAS data over the same time period to find best-fitting parameters of $a = 1.69^{+0.07}_{-0.06}$ mJy, $\tau_{decay} = 147^{+11}_{-10}$ days, and $c = 0.22 \pm 0.02$ mJy. This model is shown in Fig. 2, and it also provides a reasonable description of the data, with RMS residuals of 0.15 mJy. The best-fitting $\tau_{decay} \sim 147$ d is roughly three times longer than found for typical TDEs (Holoien et al. 2014a, 2016a, b). The exponential decay fit is also a better description of the data than a $t^{-5/3}$ decline.

We next compare the RMS measurements obtained from the decline fits to the RMS scatter in the archival ATLAS light curve. Only considering data taken before the beginning of the rise on MJD $\simeq$ 58110, we find an RMS scatter of 0.02 mJy in the ATLAS o-band data, suggesting that the transient is significantly more variable than the host galaxy was in quiescence.

### 3.2 TESS light curve

With our *TESS* light curve, we are able to study the variability properties of ASASSN-18el in great detail. In order to understand,

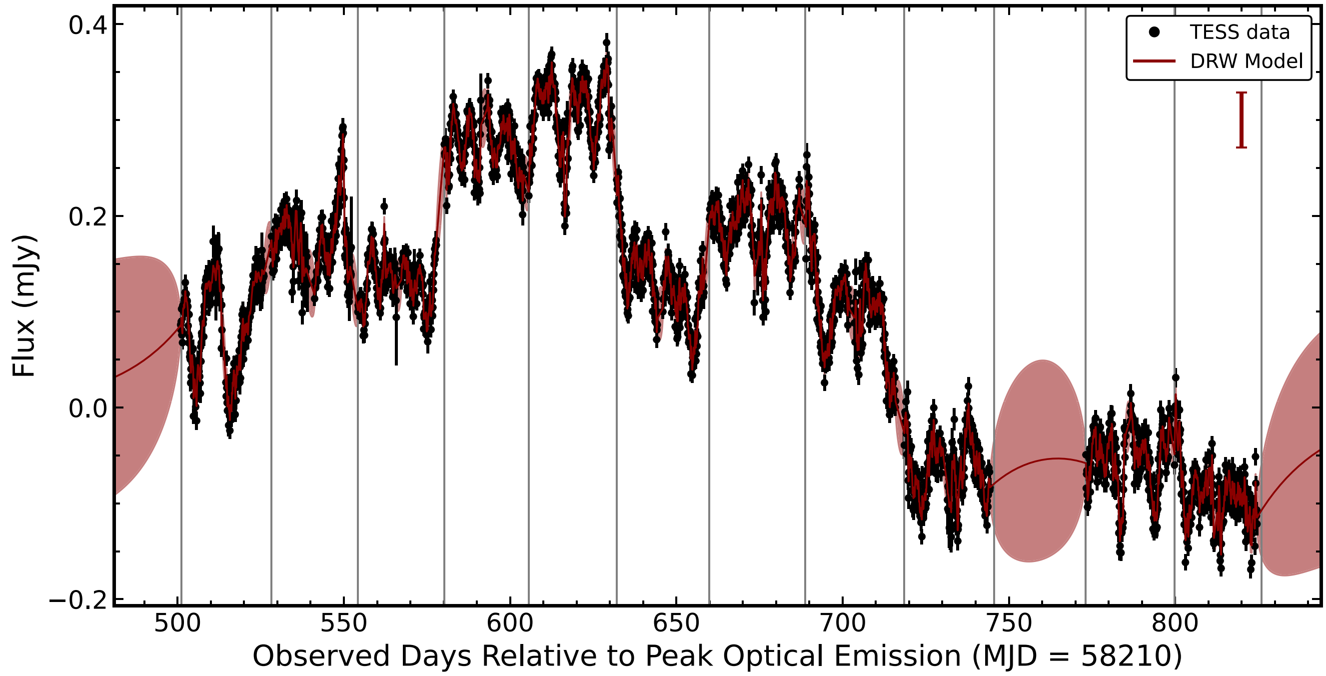


**Figure 3.** *TESS* data stacked in 2-h bins (black points) with the mean DRW light curve shown in red. In this model, linear offsets are computed between the sectors such that the global mean flux is zero. Here, no correction for Galactic extinction has been applied. The shading represents the RMS of the DRW light curves. The range of allowed light curves broadens rapidly when there is no data in a given time interval. The vertical grey bars mark the beginning of new sectors. The inter-sector calibration has larger errors than the point-to-point precision in the *TESS* light curve (shown as the error bar in the upper right), but these uncertainties are included in our analysis and do not affect our results.

this variability in the context of AGN, we used a damped-random-walk (DRW) model (e.g. Kelly, Bechtold & Siemiginowska 2009; Kozłowski et al. 2010; MacLeod et al. 2010; Zu, Kochanek & Peterson 2011; MacLeod et al. 2012; Zu et al. 2013) to fit the variability seen in Fig. 3. Fundamentally, a DRW variability model assumes that the power spectral density (PSD) of an AGN can be described by a flat spectrum (white noise) at low frequencies, with a smooth transition to a $f^{-2}$ power-law (red noise) at higher frequencies. The parameters of the model are the characteristic time-scale $\tau_{DRW}$ and the amplitude $\hat{\sigma} = \sigma[(2 \times 365.25\ \mathrm{d})/\tau_{DRW}]^{1/2}$.

Following Kozłowski et al. (2010), we fit the observed *TESS* light curve from Sectors 15 to 26, allowing for an independent flux offset for each sector (these are simply additional linear parameters in the model). This provides a well-defined statistical means of including the non-adjacent data in Sectors 25–26, drives the mean flux to zero, and includes all the uncertainties from these flux offsets into the estimates of $\hat{\sigma}$ and $\tau_{DRW}$. The magnitude of the median offset is 57 $\mu$Jy with a dispersion of 83 $\mu$Jy. We binned our *TESS* light curve in 2-h bins so that the light curve has a reasonable signal-to-noise ratio per binned epoch. Throughout the remainder of this manuscript, we use these flux offsets to calibrate the fluxes for each individual Cycle 2 sector relative to the first *TESS* sector. However, we note that the inter-sector calibration likely has larger errors than the point-to-point precision in the *TESS* light curve and long time-scale trends should be viewed with caution.

The error contours for the variability time-scale and amplitude are shown in Fig. 4, with the parameters corrected for source redshift and Galactic extinction. At the 1$\sigma$ level, the contours are well-behaved, but the allowed upper bound on $\tau_{DRW}$ increases rapidly at higher confidence. The characteristic time-scale of $\tau_{DRW} = 20^{+15}_{-6}$ d is similar to those found for other AGNs with similar mass SMBHs (e.g. Kelly et al. 2009; Burke et al. 2021). The variability amplitude

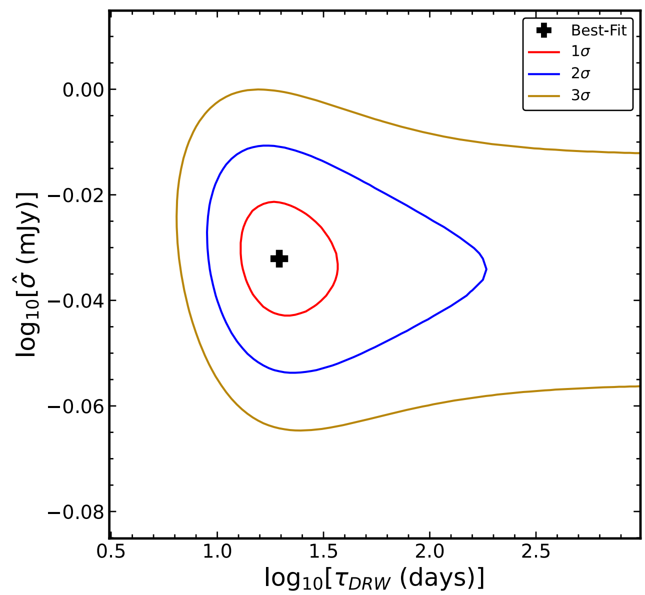


**Figure 4.** Contours of log($\hat{\sigma}$) and log($\tau_{DRW}$), shown at 1, 2, and 3$\sigma$ from the best-fitting value shown as a black cross. The values of $\hat{\sigma}$ and $\tau$ have been corrected into the rest frame using the host redshift of z = 0.01905 and $\hat{\sigma}$ has been corrected for Galactic extinction.

of $\hat{\sigma} = 0.93 \pm 0.02$ mJy, corresponding to $\sigma \sim 0.13$ mJy for $\tau_{DRW} = 20$ d, is large, immediately suggestive of AGN-like variability (e.g. Vanden Berk et al. 2004; MacLeod et al. 2010; Kozłowski 2016).

We tested how our decisions on connecting individual *TESS* sectors together affected our results, finding that regardless of how we match

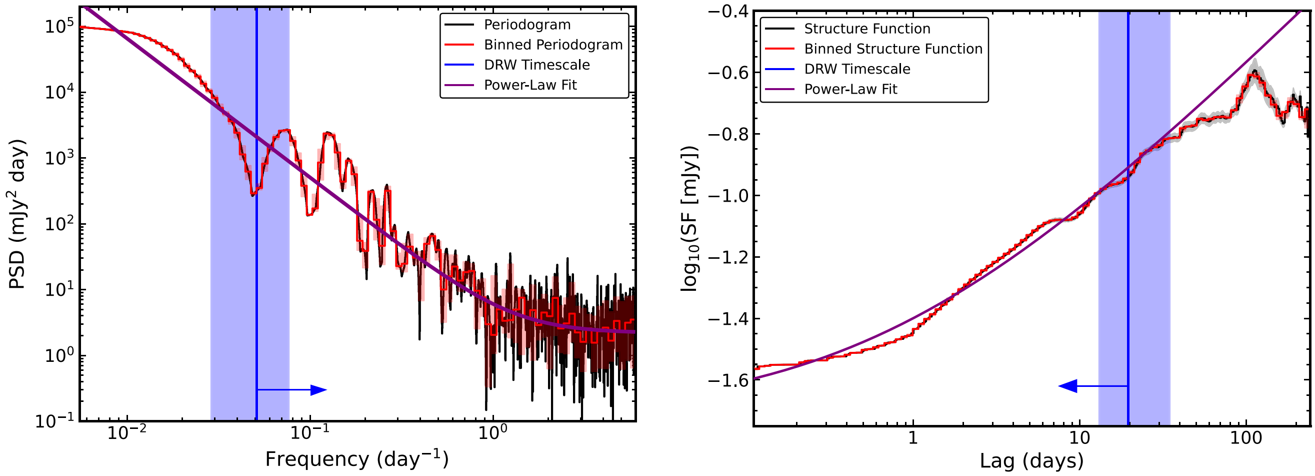


**Figure 5.** PSD (left-hand panel) and SF (right-hand panel) of the 2-h binned *TESS* light curve. The PSD is computed using SCIPY.SIGNAL.PERIODOGRAM. The red lines are the PSD and SF binned in 100 logarithmic bins and the red shading indicates the $1\sigma$ scatter over that bin width. The grey band around the SF is the uncertainty at that lag. The blue lines are the estimated $\tau_{DRW}$, with the shading representing the uncertainty. As expected, the best-fitting $\tau_{DRW}$ roughly coincides with the break in the PSD from a flat white noise to the higher frequency power-law slope. The purple lines are a power-law fits, with the PSD fit giving $\alpha = -2.11$ and the SF fit yielding $\gamma = 0.54$, both consistent with the expectations of a DRW model. The blue arrows represent the regions over which the power-law fits are done.

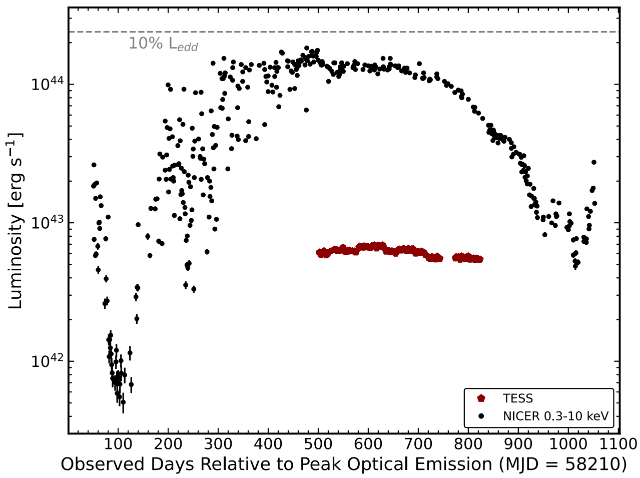


**Figure 6.** NICER (black circles) and *TESS* (dark red pentagons) light curves of ASASSN-18el. The NICER luminosity is integrated over the 0.3–10 keV bandpass. The *TESS* luminosity is $\lambda L_\lambda$ at the pivot wavelength of the *TESS* bandpass and includes the quiescent host galaxy plus AGN flux. It is clear that the X-ray component of the emission is more than an order of magnitude more luminous than the optical component during the time of overlapping data.

adjoining sectors, the recovered $\tau_{DRW}$ values are consistent within $1\sigma$ uncertainties. The variability amplitude $\sigma$ is much more sensitive to choices on sector matching, but we are able to directly compute the RMS scatter for each *TESS* sector, circumventing the DRW modelling and sector-matching entirely. The median RMS scatter per sector is 24 $\mu$Jy, which is 8 per cent of the median *TESS* flux over the same range.

Fig. 5 shows the PSD and structure function (SF) of the TESS light curve of ASASSN-18el between Sectors 15 and 23, avoiding the sector-long gaps in the *TESS* coverage. The PSD was computed using SCIPY.SIGNAL.PERIODOGRAM and a flat top window function to increase amplitude accuracy. As expected from previous studies of AGN variability (e.g. Mushotzky et al. 2011; Kozłowski 2017), the PSD is flat at low frequencies, with a declining power-law at higher frequencies. Similarly, the SF is roughly flat at long lags with a declining slope towards shorter lags. At the highest frequencies (shortest lags), the PSD (SF) flattens again as the signal becomes dominated by photometric noise. There is also a dip in the PSD at $\sim$0.04 d$^{-1}$, likely due to the 27 d length of the *TESS* sector and the linear offsets applied between the sectors. If we fit the PSD above the measured value of $\tau_{DRW}$ (in frequency) with a single power-law plus a photometric noise term, we find a power-law index of $\alpha = -2.11 \pm 0.16$. Likewise, if we fit the SF below the measured value of $\tau_{DRW}$ (in time) with the same model, we find a power-law index of $\gamma = 0.54 \pm 0.02$.

The canonical power-law slope for a DRW model is $\alpha = -2$ (e.g. Zu et al. 2011; Zu et al. 2013) for the PSD and $\gamma = 0.5$ (e.g. Kozłowski 2016) for the SF. Studies of AGNs using high-quality Kepler light curves (Mushotzky et al. 2011; Smith et al. 2018) have shown a range of power-law slopes between $\alpha = -1.7$ and $\alpha = -3.3$, although Moreno et al. (2021) showed that Kepler systematics can mimic AGN variability. Therefore, we find that the power-law slopes for the PSD and SF of ASASSN-18el are fully consistent with other optical AGNs and with the theoretical assumptions made when fitting the *TESS* light curve with a DRW model.

### 3.3 Optical/X-ray correlation

Next, we searched for a correlation between the *TESS* optical and NICER X-ray light curves, shown in Fig. 6. Here, we include the quiescent host galaxy plus AGN flux in the *TESS* bandpass to the zero-mean *TESS* light curve shown in Fig. 3. The X-ray emission is roughly an order of magnitude higher than the optical emission at the same phase, unlike many other ANTs (Neustadt et al. 2020; Hinkle et al. 2021a). Qualitatively, both light curves show a plateau over the time period from 500 to 700 d after the peak emission where they overlap.

We tried to measure a temporal lag between the NICER and *TESS* light curves. If the optical variability was a result of the reprocessing of the far more luminous X-rays, we would expect to see a correlation

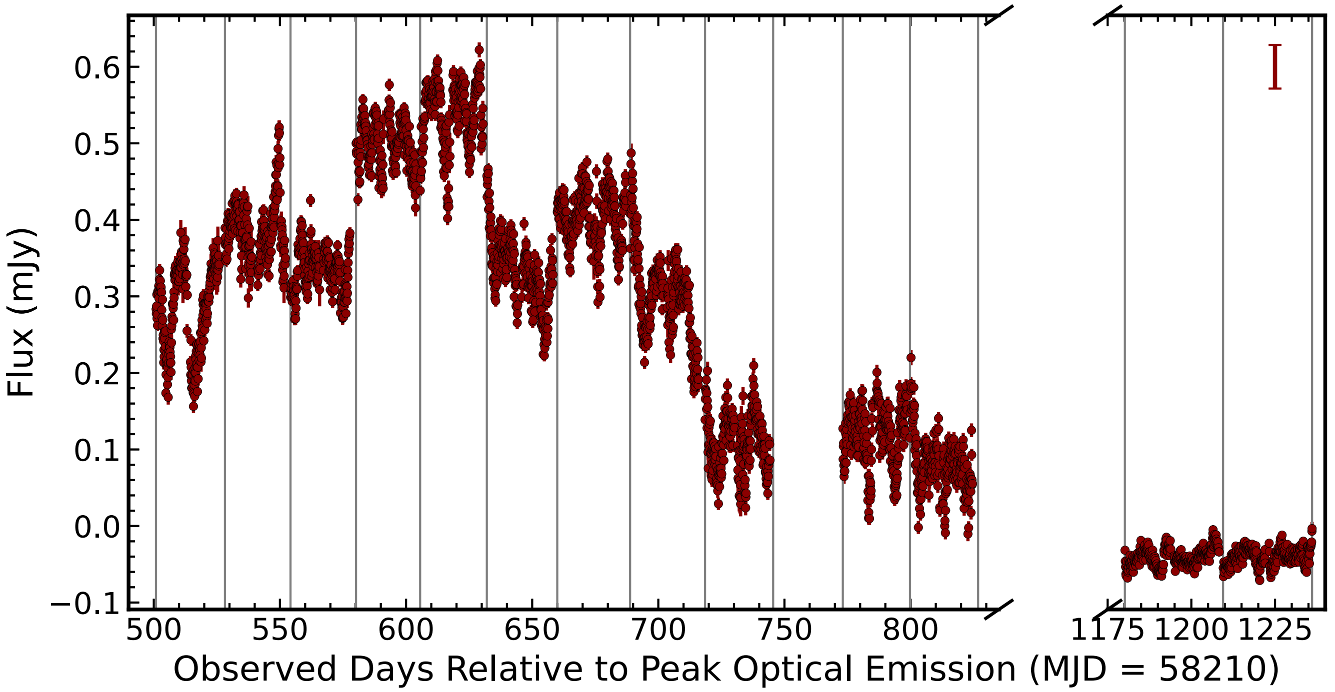


**Figure 7.** *TESS* data stacked in 2 h bins (red points) spanning from the initial Sector 15 light curve to the very late-time Sector 41 light curve. The vertical grey bars mark the beginning of new sectors, and the error bar in the upper right indicates the median magnitude of the sector-to-sector offsets. Shown for *TESS* sectors prior to Sector 40 is the zero-mean DRW light curve from Fig. 3 scaled such that the first *TESS* sector matches the differential flux in concurrent ATLAS o-band data. For the very late-time sectors, the *TESS* light curve is scaled to match the differential flux in concurrent ATLAS o-band data.

between light curve features in the X-ray and the optical, with the optical lagging behind the X-ray. Assuming this is due to light travel time, this lag would give an approximate physical size of the accretion disc between the X-ray emitting corona and the cooler portions of the disc from which the emission seen in the *TESS* bandpass originate. Unfortunately, neither the straightforward cross-correlation function code PyCCF (Sun, Grier & Peterson 2018) nor the more sophisticated DRW modelling code JAVELIN (Zu et al. 2011; Zu et al. 2013) model produced a useful result. Additionally, we tested if binning the *TESS* data and/or smoothing the light curves to remove long-term trends affected the lag fits, but neither was able to return an acceptable result.

### 3.4 Very late-time data

After *TESS* returned to the Northern hemisphere in Cycle 4, ASASSN-18el was observed again. We show the full *TESS* light curve as of the end of 2021, including Sectors 15–23, 25–26, and 40–41 in Fig. 7. It is immediately clear that the rapid high-amplitude variability has faded by the very-late time sectors. To quantify the change in variability amplitude between the early and late sectors, we measured the RMS scatter in the first sector and compared it to the last sector. For Sector 15, the RMS scatter around the median flux is 46 $\mu$Jy. Roughly 2 yr later in Sector 41, the RMS scatter had dropped by a factor of almost 5–9 $\mu$Jy. ASASSN-18el will be observed in 13 continuous *TESS* sectors in Cycles 4 and 5 (Sectors 47–59), allowing for additional late-time monitoring of the source variability well after the transient has faded.

While the overall light curve shape is not particularly important for understanding the short-term variability expected of AGNs, we used stacked late-time ATLAS data to measure the $o$-band flux concurrent with active *TESS* sectors to allow us to create a long-term *TESS* light curve. We matched the first *TESS* sector to the concurrent ATLAS $o$-band flux and applied the linear offsets between sectors computed in the DRW modelling to calibrate the flux of the remaining Cycle 2 *TESS* sectors. For the Cycle 4 *TESS* light curves, we added the concurrent ATLAS $o$-band flux to the differential *TESS* light curve. As our primary aim in Fig. 7 is to show the consistent strong short-term variability of ASASSN-18el over a 2 yr time span, details on sector-to-sector matching are largely inconsequential.

## 4 DISCUSSION

Two plausible explanations have been put forward to explain the CL phenomenon observed for the ANT ASASSN-18el. The first is related to instabilities in the existing AGN disc, either as a result of a change in the accretion flow (Trakhtenbrot et al. 2019b) or something more exotic like a magnetic inversion in the disc (Scepi, Begelman & Dexter 2021; Laha et al. 2022). The second is increased accretion due to a TDE, which disrupted the existing X-ray corona while powering a large UV/optical flare (Ricci et al. 2020; Li et al. 2022; Masterson et al. 2022).

The variability seen in the *TESS* light curve is typical of known AGNs and consistent with the DRW model frequently used to describe AGN variability. Both the PSD and SF of the *TESS* light curve are typical of AGNs. Therefore, independent of any modelling of the *TESS* light curve and choices on sector matching, this short-term stochastic variability suggests an AGN origin for ASASSN-18el.

Nevertheless, with a measurement of $\tau_{DRW}$, we can compare to known relationships, such as the one between $\tau_{DRW}$ and the central SMBH mass, shown in Fig. 8. As the black hole mass increases, so does the characteristic time-scale, resulting from the scaling of accretion disc parameters (e.g. Kelly et al. 2009; Zu et al. 2013).

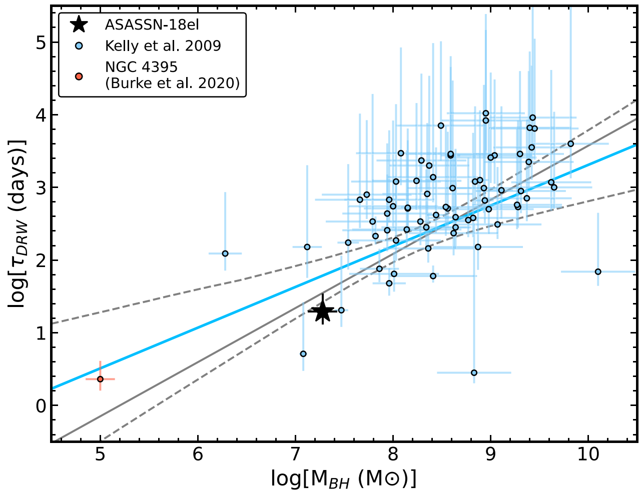


**Figure 8.** The rest-frame DRW time-scale ($\tau_{DRW}$) as compared to the SMBH mass for a given AGN. The sample of Kelly et al. (2009) is shown in light blue, with their best-fitting line shown with the light blue solid line. The solid grey line is our fit of the Kelly et al. (2009) sample using the methods of Kelly (2007). The dashed grey lines are plus/minus 1$\sigma$ from the best-fitting line. Both NGC 4395 (Burke et al. 2020) and ASASSN-18el are excluded from this fit.

In particular, Burke et al. (2021) suggest that the characteristic variability time-scale is linked to the thermal time-scale for the UV-emitting region of the accretion disc, even when that $\tau_{DRW}$ is measured with optical rather than UV photometry. ASASSN-18el lies near the trend between $\tau_{DRW}$ and SMBH mass. In Fig. 8, we have shown both the original best-fitting line and our fit to the data from Kelly et al. (2009) using the MCMC procedure of Kelly (2007) to better illustrate the range of allowed slopes for this relationship given many sources with large uncertainties.

Similarly, we can compare the pre-flare constraints from ASAS-SN and ATLAS on variability to those obtained with *TESS*. Prior to the flare, there are only hints of weak activity, with sparse detections in the ASAS-SN *V*-band photometry. This is consistent with the archival Seyfert 2 classification of the AGN 1ES 1927 + 654. The lack of strong variability prior to the flare in contrast with short-time-scale variability seen during the flare suggests that ASASSN-18el is an example of an increase in the accretion rate onto the AGN rather than a TDE. This scenario is also consistent with the late-time decrease in variability, as the AGN begins to return to its quiescent state.

It is important to note that there are some caveats to the analysis of AGN light curves using a DRW model. The primary concern is the length of the light-curve relative to the recovered time-scale. Recent simulations suggest that for robust recovery of DRW parameters, the length of the light curve should be at least 10 times the $\tau_{DRW}$ (e.g. Kozłowski 2017, 2021), with shorter light curves biased towards shorter time-scales. For ASASSN-18el, the length of the *TESS* light curve is roughly 16 times longer than the recovered $\tau_{DRW}$. Fig. 4 of Kozłowski (2021) suggests that there is only a ∼0.1 dex uncertainty in $\tau_{DRW}$ at this length. Even if the true $\tau_{DRW}$ for ASASSN-18el was underestimated by a few tenths of a dex, it would remain close to the trend shown in Fig. 8. Finally, as noted in Section 3.2, results related to the long-time-scale trends in the *TESS* light curve should be viewed with caution because of uncertainties and systematic issues associated with the inter-sector calibrations.

In addition to the high precision *TESS* photometry, the X-ray light curve from NICER gives important constraints on physical processes occurring close to the SMBH. Two notable aspects of the X-ray emission for ASASSN-18el are the extremely high X-ray to optical luminosity ratio and the deep dip in X-ray flux at ∼100 d after the optical peak. The proposed model of Scepi et al. (2021) may provide a natural explanation for these features. In this model, the accretion disc prior to the flare exists in a magnetically arrested disc (MAD) state (e.g. Narayan, Igumenshchev & Abramowicz 2003). In such a state, the UV/optical region of the disc is radiatively inefficient and the X-ray emission is synchrotron-powered (Scepi et al. 2021), accounting for the unusually high X-ray to optical luminosity ratio.

Scepi et al. (2021) suggest that a magnetic inversion occurs due to the advection of material with opposite magnetic polarity through the disc, thus disrupting the MAD state. In such a magnetic inversion, reconnection occurs first in the outer regions of the disc, increasing the radiative efficiency and powering the dramatic UV/optical flare. As the accretion flow reaches the SMBH, the X-ray corona is destroyed, decreasing the X-ray luminosity with a lag relative to the UV/optical brightening (Scepi et al. 2021). As magnetic flux accumulates, the X-ray corona is rebuilt and the X-ray luminosity recovers. The decline in the UV/optical emission can either be due to a newly formed MAD state or a decrease in the accretion rate. Scepi et al. (2021) predict that for the latter scenario, we should see a secondary decline in the X-ray luminosity roughly 2 yr later. Indeed, the NICER data show a decline in X-ray luminosity beginning at ∼700 d after peak optical emission, consistent with such a model.

Finally, with respect to the possibility that the CL phenomenon was caused by a TDE, it is difficult to explain the observed variability in the context of TDE emission. To date, only a small number of TDEs have exhibited any stochastic variability (e.g. Holoien et al. 2019), and TDE light curves rarely exhibit re-brightening episodes (e.g. Malyali et al. 2023; Wevers et al. 2023) like the ones seen here in ATLAS and ASAS-SN photometry. Late-time studies of TDEs have suggested a shift in the emission mechanism from one tied to the fallback of mass onto the SMBH to emission from the accretion disc itself (Balbus & Mummery 2018; van Velzen et al. 2019; Jonker et al. 2020). A natural assumption is that, similar to AGN discs, this may lead to enhanced variability from instabilities in disc. None the less, when examining late-time data on the TDEs ASASSN-14ae and ASASSN-14li (van Velzen et al. 2019; Hinkle et al. 2021c), we find that there is no significant variability on several day time-scales even long after disc emission is thought to become the dominant component for these sources (van Velzen et al. 2019). This suggests that a TDE transitioning to a disc-dominated state is unlikely to show the very large variability that we see from ASASSN-18el at similarly late times. In addition, the long overall time-scale of the event is not consistent with known TDEs (e.g. Holoien et al. 2014a, 2016a, b; Hinkle et al. 2020). These suggest that a TDE is likely not the source of the transient emission for ASASSN-18el.

## 5 SUMMARY

Through our analysis of late-time optical photometry, NICER X-ray data, and a high-cadence TESS light curve of ASASSN-18el, we find the following:

(i) Optical transient emission from ASASSN-18el remains detectable above pre-flare levels for roughly 700 d after the peak optical emission with late-time re-brightening episodes continuing until at least 1250 d after peak.

(ii) The initial decline of ASASSN-18el as measured from the ATLAS *o*-band light curve is significantly flatter than the canonical $t^{-5/3}$ power-law for TDEs. Additionally, when the decline is fit by an exponential-decay model, the time-scale of the decline is roughly three times longer than observed for typical TDEs.

(iii) The high-S/N and high-cadence *TESS* light curve within 1000 d of peak optical emission shows strong variability on time-scales less than a single *TESS* sector, immediately suggestive of strong AGN activity.

(iv) The *TESS* light curve's large variability amplitude and characteristic time-scale are consistent with light curves of AGNs with similar SMBH masses, supporting the claim that the observed transient emission at late times is fully consistent with a dramatic AGN flare. However, there are large uncertainties and potential systematic errors related to the long-time-scale trends in the *TESS* light curve.

(v) The X-ray and optical evolution is distinct, with large dips in X-ray luminosity at early and late times despite a relatively smooth optical light curve. However, during the period of overlap between TESS and NICER data, a multiwavelength plateau phase is observed. None the less, we were unable to recover a temporal lag between the X-ray and *TESS* bandpasses.

(vi) The very late-time *TESS* data (more than 1000 d after peak emission) continues to show stochastic variability, but at a lower amplitude than earlier sectors.

From our analysis of these late-time data, and in particular the exquisite *TESS* data, we find that the flare in ASASSN-18el is likely the result of a large AGN flare, possibly induced by a magnetic inversion in the disc (Scepi et al. 2021). Many of the optical CL-AGNs to date lack the wealth of data presented here. However, the few that do, such as NGC 2617 (Shappee et al. 2014) and ASASSN-18el, may suggest that such state changes are not always long term but rather may be the result of large flares.

The use of *TESS* and its unparalleled combination of photometric precision, cadence, and sky coverage is a promising avenue for studying the physical origin of ANTs. TESS observations of an ANT at any phase can give detailed insight into the variability properties of a galaxy. At the very least, a sector of *TESS* data should be able to uncover the presence of AGN-like variability in ANT host galaxies, well below what can be probed from the ground. This gives promise that we can begin to understand the range of nuclear behaviours and accretion processes through the disambiguation of ANTs.

## ACKNOWLEDGEMENTS

We thank the referee for helpful comments and suggestions that have greatly improved the quality of this manuscript. We also thank Alexa Anderson and Willem Hoogendam for useful comments on the manuscript.

We thank Las Cumbres Observatory and its staff for their continued support of ASAS-SN. ASAS-SN is funded in part by the Gordon and Betty Moore Foundation through grants GBMF5490 and GBMF10501 to the Ohio State University and the Alfred P. Sloan Foundation grant G-2021-14192. Development of ASAS-SN has been supported by NSF (National Science Foundation) grant AST-0908816, the Mt. Cuba Astronomical Foundation, the Center for Cosmology and AstroParticle Physics at the Ohio State University, the Chinese Academy of Sciences South America Center for Astronomy (CAS- SACA), the Villum Foundation, and George Skestos.

JTH was supported by NASA (National Aeronautics and Space Administration) grant 80NSSC21K0136. BJS and CSK are supported by NSF grant AST-1907570/AST-1908952. BJS is also supported by NSF grants AST-1920392 and AST-1911074. CSK is supported by NSF grant AST-181440. TAT is supported in part by NASA grant 80NSSC20K0531.

Parts of this research were supported by the Australian Research Council Centre of Excellence for All Sky Astrophysics in 3 Dimensions (ASTRO 3D), through project number CE170100013.

BSG was supported by Thomas Jefferson Chair for Discovery and Space Exploration at the Ohio State University.

DEMONEXT was supported by NSF CAREER Grant AST-1056524 and the Vanderbilt Initiative in Data-intensive Astrophysics (VIDA).

This work is based on observations made by ASAS-SN and ATLAS. The authors wish to recognize and acknowledge the very significant cultural role and reverence that the summit of Haleakalā has always had within the indigenous Hawaiian community. We are most fortunate to have the opportunity to conduct observations from this mountain.

## DATA AVAILABILITY

The data underlying this article will be shared on reasonable request to the corresponding author.

## REFERENCES

Alard C., 2000, A&AS, 144, 363
Alard C., Lupton R. H., 1998, ApJ, 503, 325
Auchettl K., Guillochon J., Ramirez-Ruiz E., 2017, ApJ, 838, 149
Balbus S. A., Mummery A., 2018, MNRAS, 481, 3348
Barron J. T., Stumm C., Hogg D. W., Lang D., Roweis S., 2008, AJ, 135, 414
Bennett C. L., Larson D., Weiland J. L., Hinshaw G., 2014, ApJ, 794, 135
Bianchi S., Guainazzi M., Matt G., Chiaberge M., Iwasawa K., Fiore F., Maiolino R., 2005, A&A, 442, 185
Bogdanov S. et al., 2019, ApJ, 887, L25
Boller T. et al., 2003, A&A, 397, 557
Brown T. M. et al., 2013, PASP, 125, 1031
Burke C. J., Shen Y., Chen Y.-C., Scaringi S., Faucher-Giguere C.-A., Liu X., Yang Q., 2020, ApJ, 899, 136
Burke C. J. et al., 2021, Science, 373, 789
Denney K. D. et al., 2014, ApJ, 796, 134
Drake A. J. et al., 2009, ApJ, 696, 870
Evans C. R., Kochanek C. S., 1989, ApJ, 346, L13
Frederick S. et al., 2019, ApJ, 883, 31
Frederick S. et al., 2021, ApJ, 920, 56
Gendreau K. C., Arzoumanian Z., Okajima T., 2012, SPIE, 8443, 844313
Gezari S. et al., 2012, Nature, 485, 217
Giacconi R. et al., 1979, ApJ, 230, 540
Guo H. et al., 2020, ApJ, 905, 52
Haggard D., Green P. J., Anderson S. F., Constantin A., Aldcroft T. L., Kim D.-W., Barkhouse W. A., 2010, ApJ, 723, 1447
Henden A. A., Levine S., Terrell D., Welch D. L., 2015, AAS Meeting #225. American Astronomical Society, p. 336.16
Hinkle J. T., Holoien T. W. S., Shappee B. J., Auchettl K., Kochanek C. S., Stanek K. Z., Payne A. V., Thompson T. A., 2020, ApJ, 894L, 10
Hinkle J. T. et al., 2021a, ApJ, 930, 12
Hinkle J. T. et al., 2021b, MNRAS, 500, 1673
Hinkle J. T., Holoien T. W. S., Shappee B. J., Auchettl K., 2021c, ApJ, 910, 83
Ho L. C., 2008, ARA&A, 46, 475
Holoien T. W.-S. et al., 2014a, MNRAS, 445, 3263
Holoien T. W.-S. et al., 2014b, ApJ, 785, L35
Holoien T. W.-S. et al., 2016a, MNRAS, 455, 2918

Holoien T. W.-S. et al., 2016b, MNRAS, 463, 3813
Holoien T. W.-S. et al., 2019, MNRAS, 484, 1899
Holoien T. W. S. et al., 2020, ApJ, 898, 161
Holoien T. W. S. et al., 2021,ApJ, 933, 196
Jonker P. G., Stone N. C., Generozov A., van Velzen S., Metzger B., 2020, ApJ, 889, 166
Kelly B. C., 2007, ApJ, 665, 1489
Kelly B. C., Bechtold J., Siemiginowska A., 2009, ApJ, 698, 895
Kochanek C. S. et al., 2017, PASP, 129, 104502
Kozłowski S., 2016, ApJ, 826, 118
Kozłowski S., 2017, A&A, 597, A128
Kozłowski S., 2021, AcA, 71, 103
Kozłowski S. et al., 2010, ApJ, 708, 927
LaMassa S. M. et al., 2015, ApJ, 800, 144
Lacerda E. A. D., Sánchez S. F., Cid Fernandes R., López-Cobá C., Espinosa-Ponce C., Galbany L., 2020, MNRAS, 492, 3073
Laha S. et al., 2022, ApJ, 931, 5
Lang D., Hogg D. W., Mierle K., Blanton M., Roweis S., 2010, AJ, 139, 1782
Leloudas G. et al., 2019, ApJ, 887, 218
Li R., Ho L. C., Ricci C., Trakhtenbrot B., Arcavi I., Kara E., Hiramatsu D., 2022, ApJ, 933, 70
Lupton R., 2005, http://www.sdss.org/dr5/algorithms/sdssUBVRITransform.html
MacLeod C. L. et al., 2010, ApJ, 721, 1014
MacLeod C. L. et al., 2012, ApJ, 753, 106
Malyali A. et al., 2021, A&A, 647, A9
Malyali A. et al., 2023, MNRAS, 520, 3549
Masterson M. et al., 2022, ApJ, 934, 35
Moreno J., Buttry R., O'Brien J., Vogeley M. S., Richards G. T., Smith K. L., 2021, AJ, 162, 232
Mushotzky R. F., Edelson R., Baumgartner W., Gandhi P., 2011, ApJ, 743, L12
Narayan R., Igumenshchev I. V., Abramowicz M. A., 2003, PASJ, 55, L69
Neustadt J. M. M. et al., 2020, MNRAS, 494, 2538
Nicholls B. et al., 2018, Astron. Telegram, 11391, 1
Payne A. V. et al., 2021, ApJ, 910, 125
Phinney E. S., 1989, Nature, 340, 595
Rees M. J., 1988, Nature, 333, 523
Ricci C. et al., 2017, ApJS, 233, 17
Ricci C. et al., 2020, ApJ, 898, L1
Ricci C. et al., 2021, ApJS, 255, 7
Ricker G. R. et al., 2015, J. Astron. Telesc. Instrum. Syst., 1, 014003
Scepi N., Begelman M. C., Dexter J., 2021, MNRAS, 502, L50
Schlafly E. F., Finkbeiner D. P., 2011, ApJ, 737, 103
Shappee B. J. et al., 2014, ApJ, 788, 48
Smith K. L., Mushotzky R. F., Boyd P. T., Malkan M., Howell S. B., Gelino D. M., 2018, ApJ, 857, 141
Smith K. W. et al., 2020, PASP, 132, 5002
Sun M., Grier C. J., Peterson B. M., 2018, Astrophysics Source Code Library, record ascl:1805.032
Tonry J. L. et al., 2018a, PASP, 130, 064505
Tonry J. L. et al., 2018b, ApJ, 867, 105
Trakhtenbrot B. et al., 2019a, Nature Astron., 3, 242
Trakhtenbrot B. et al., 2019b, ApJ, 883, 94
Tran H. D., Lyke J. E., Mader J. A., 2011, ApJ, 726, L21
Ulrich M.-H., Maraschi L., Urry C. M., 1997, ARA&A, 35, 445
Vallely P. J. et al., 2019, MNRAS, 487, 2372
Vallely P. J., Kochanek C. S., Stanek K. Z., Fausnaugh M., Shappee B. J., 2021, MNRAS, 500, 5639
Vanden Berk D. E. et al., 2004, ApJ, 601, 692
Vanderspek R., Doty J., Fausnaugh M., Villaseñor J., Jenkins J., Berta-Thompson Z., Burke C., Dreyer S., Ricker G., 2018, Technical Report, TESS Instrument Handbook, Kavli Institute for Astrophysics and Space Science, Massachusetts Institute of Technology
van Velzen S. et al., 2011, ApJ, 741, 73
van Velzen S., Stone N. C., Metzger B. D., Gezari S., Brown T. M., Fruchter A. S., 2019, ApJ, 878, 82
van Velzen S. et al., 2021, ApJ, 908, 4
Vaughan S., Edelson R., Warwick R. S., Uttley P., 2003, MNRAS, 345, 1271
Villanueva S., Eastman J. D., Gaudi B. S., Pogge R. W., Stassun K. G., Trueblood M., Trueblood P., 2016, in Hall H. J., Gilmozzi R., Marshall H. K.eds, SPIE Conf. Ser., Vol. 9906, Ground-Based and Airborne Telescopes VI. SPIE, Bellingham, p. 99062L
Villanueva Steven J., Gaudi B. S., Pogge R. W., Eastman J. D., Stassun K. G., Trueblood M., Trueblood P., 2018, PASP, 130, 015001
Wevers T. et al., 2023, ApJ, 942, L33
Wright E. L., 2006, PASP, 118, 1711
Wyrzykowski Ł. et al., 2017, MNRAS, 465, L114
Zu Y., Kochanek C. S., Peterson B. M., 2011, ApJ, 735, 80
Zu Y., Kochanek C. S., Kozłowski S., Udalski A., 2013, ApJ, 765, 106

This paper has been typeset from a TeX/LaTeX file prepared by the author.